


UPCommons


Portal del coneixement obert de la UPC

<http://upcommons.upc.edu/e-prints>

Publicat sota llicència de la IOP Publishing Ltd. a *Journal of Physics: Conference Series*

 El contingut d'aquest treball pot ser utilitzat sota els termes de la llicència Creative Commons Reconeixement 3.0. Qualsevol distribució addicional d'aquest treball ha de mantenir l'atribució de l'autor/s i el títol de l'obra, la citació de la publicació i el DOI.

Published under licence in *Journal of Physics: Conference Series* by IOP Publishing Ltd.

 Content from this work may be used under the terms of the Creative Commons Attribution 3.0 licence. Any further distribution of this work must maintain attribution to the author(s) and the title of the work, journal citation and DOI.

Numerical simulation of roughness effects on the flow past a circular cylinder

I. Rodríguez¹, O. Lehmkuhl¹, U. Piomelli², J. Chiva¹, R. Borrell¹ and A. Oliva¹

¹ Universitat Politècnica de Catalunya, Colom 11 08222, Terrassa (Barcelona), Spain

² Department of Mechanical and Materials Engineering, Queen's University, Kingston, Ontario K7L 3N6, Canada

E-mail: ivette@cttc.upc.edu

Abstract. In the present work large eddy simulations of the flow past a rough cylinder are performed at a Reynolds number of $Re = 4.2 \times 10^5$ and an equivalent sand-grain surface roughness height $k_s = 0.02$, in order to determine the effects of the surface roughness on the boundary layer transition and as a consequence on the wake topology. For comparison, results are compared to that of the smooth cylinder. It is shown that surface roughness triggers an earlier transition in the boundary layer, thus leading to an earlier separation caused by the increased drag and momentum deficit. As a consequence, the drag coefficient increases from about $C_D \approx 0.3$ to $C_D \approx 1.122$. The wake topology at this Reynolds number also changes and resembles more the subcritical wake observed for the smooth cylinder at lower Reynolds numbers.

1. Introduction

The flow over smooth cylinders has been extensively studied; it is associated with various instabilities that involve the boundary layer, the separated shear layers and the wake. A comprehensive description of the flow phenomena at different Reynolds numbers (Re) can be found in [1]. It is well known that when Reynolds numbers is about 2×10^5 major changes occur in the flow configuration as the drag coefficient rapidly decreases (see Fig. 1). This phenomenon is known as the 'drag crisis'. In addition to the steep drop in the drag, the appearance of a small laminar bubble separation (LSB) on the cylinder surface is also a characteristic of the flow pattern at critical and super-critical Reynolds numbers. The combination of a decrease in the pressure minimum and an increase in the back pressure results in an adverse pressure gradient leading to the detachment of the boundary layer; transition to turbulence occurs just after separation. As a result, the shear-stresses, which cause the transport of the momentum in the separated boundary layer, cause the flow reattachment, and a LSB is formed. At the onset of the critical transition, the LSB on the top side of the cylinder is responsible for asymmetries in the forces acting on the cylinder and in the near wake flow. With the increase in the Reynolds number, as the flow enters the super-critical regime, a second LSB forms on the opposite side stabilizing the forces and the wake [2]. Considerable experimental work has been carried out measuring the forces acting on the cylinder at these Reynolds numbers, some examples are [3, 4, 5, 6, 7, 8].

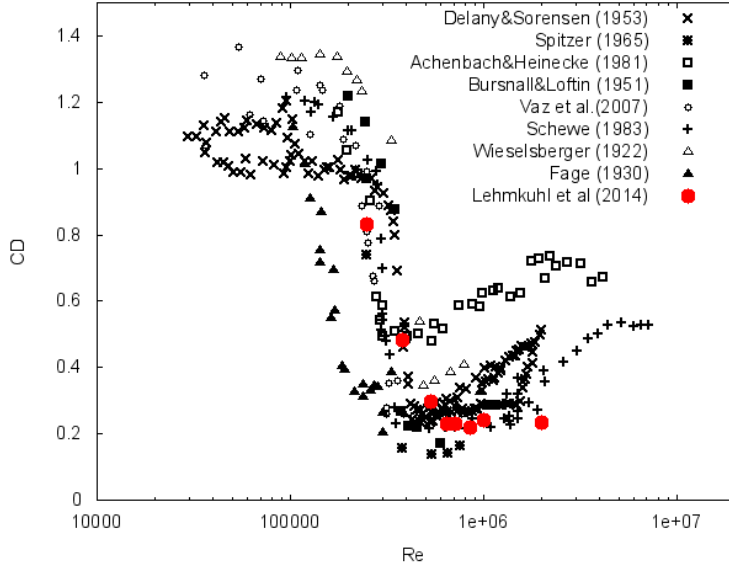


Figure 1. Critical and super-critical drag coefficient as found in the literature. Results obtained by the authors are represented by red dots and can be found in [2] and [9].

The effect of roughness, especially in turbulent boundary layers, has been focus of many research studies. A review of the literature can be found in [10, 11, 12]. Most of the investigations in this area, however, have been performed on fully developed turbulent pipes and channels, and in zero-pressure-gradient turbulent boundary layers. Roughness effects on boundary layers on curved surfaces and in particular on bluff bodies is quite limited (e.g., [?, ?]). Roughness is known to give rise to an earlier transition in a turbulent boundary layer [13, 14, 15]. For the surfaces considered by [14], for instance, roughness appears to increase the friction drag, without any beneficial effect on the separation characteristics: the onset of the critical transition (Figure 1) is shifted to lower Reynolds numbers [16], but the minimum drag coefficient is larger than that on a smooth cylinder, due to the transition to turbulence occurring at lower Reynolds numbers, and to an earlier separation due to the increased drag (and momentum deficit) caused by the roughness [13, 14, 17, 18].

In the present work an issue to be addressed is how the changes in the boundary layer affect the transition to turbulence and, as a consequence, the flow conditions behind the cylinder. To do this, the flow past a cylinder at a Reynolds number of $Re = 4.2 \times 10^5$ with a rough surface with an equivalent sand-grain surface roughness height of $k_s = 0.02$ is being studied by means of large-eddy simulations (LES). For the smooth cylinder at this Reynolds number the flow is in the critical regime, i.e. the boundary layer has transitioned to turbulence just after separation causing the reattachment of the flow and a further turbulent separation in the rear side of the cylinder, with a consequent decrease in the drag up to $C_D \approx 0.3$ [2, 9]. Thus, changes in the flow parameters, boundary layer and flow topology are analysed by means of the direct comparison with results for the smooth cylinder.

2. Mathematical and numerical models

The spatially filtered incompressible Navier-Stokes equations [19] can be written as

$$\frac{\partial \bar{u}_i}{\partial x_i} = 0 \quad (1)$$

$$\frac{\partial \bar{u}_i}{\partial t} + \frac{\partial \bar{u}_i \bar{u}_j}{\partial x_j} - \nu \frac{\partial^2 \bar{u}_i}{\partial x_j \partial x_j} + \rho^{-1} \frac{\partial \bar{p}}{\partial x_i} - F_i = -\frac{\partial \mathcal{T}_{ij}}{\partial x_j} \quad (2)$$

where x_i are the spatial coordinates (x , y and z) in the stream-wise, cross-stream and span-wise directions. \bar{u}_i and \bar{p} stand for the filtered velocity and pressure. ν is the kinematic viscosity and ρ the density of the fluid. F_i is a body force used to impose the no-slip boundary condition on the rough cylinder surface; it is non-zero in cells with roughness elements [20]. In equation (2) \mathcal{T}_{ij} is the subgrid scale (SGS) stress tensor, which must be modeled. Its deviatoric part is given by

$$\mathcal{T}_{ij} - \frac{1}{3} \mathcal{T}_{kk} \delta_{ij} = -2\nu_{sgs} \bar{\mathcal{S}}_{ij} \quad (3)$$

where $\bar{\mathcal{S}}_{ij} = \frac{1}{2}(g_{ij} + g_{ji})$ is the large-scale rate-of-strain tensor, and $g_{ij} = \partial \bar{u}_i / \partial x_j$. δ_{ij} is the Kronecker delta. The formulation is closed by an appropriate expression for the subgrid-scale viscosity, ν_{sgs} . In this project the wall-adapting local-eddy viscosity model (WALE) [21], which yielded good results in the previous simulations of the drag crisis (see [2, 9]), will be used.

The governing equations are discretized on a collocated unstructured grid arrangement using second-order spectrum-consistent schemes. Such schemes are conservative, i.e., they preserve the symmetry properties of the continuous differential operators, and ensure both stability and conservation of the kinetic-energy even at high Reynolds numbers and with coarse grids [22, 23]. For the temporal discretization of the momentum equation a self-adaptive two-step linear explicit scheme on a fractional-step method is used for the convective and diffusive terms [24], while for the pressure gradient an implicit first-order scheme is implemented. For more details about the numerical method, the user is referred to [25, 22, 23].

The Poisson system derived from the incompressibility constraint is solved using a memory-aware auto-tuned Poisson solver for problems with one Fourier diagonalizable direction. This diagonalization decomposes the original 3D system into a set of independent 2D subsystems. The algorithm focuses on optimizing the memory allocations and transactions by taking into account redundancies on such 2D subsystems. Moreover, it takes advantage of the grid uniformity in the periodic direction for its vectorization. This approach automatically optimizes the choice of the preconditioner used for the solution of each frequency subsystem and dynamically balances its parallel distribution, constituting a highly efficient and robust HPC Poisson solver. This strategy allows to involve larger number of parallel processes in a single task, with less RAM memory per parallel process [26]. The parallelization strategy will be described in more detail in the next Section.

In the present computations the boundary conditions consist of uniform velocity $(u, v, w) = (1, 0, 0)$ at the inflow, symmetry conditions at the top and bottom boundaries of the domain, while at the outlet a pressure-based condition is used. In the span-wise direction periodic boundary conditions are imposed. An immersed boundary method (IBM) is used to recover a smooth no-slip boundary condition on the rough cylinder surface. It is based on the volume-of-fluid approach, i.e. the volume fraction occupied by the fluid of each cell is evaluated in a pre-processing stage and then used in the fractional-step framework to correct the predicted velocity and enforce the no-slip condition on the rough surface [27, 20, 28].

3. Definition of the case

The flow past a rough circular cylinder at critical Reynolds numbers of $Re = 4.2 \times 10^5$ with an equivalent sand-grain surface roughness height of $k_s/D = 0.02$ is considered. Here, the Reynolds number $Re = U_{ref} D/\nu$ is defined in terms of the cylinder diameter D and the free-stream velocity U_{ref} . The main interest in this case is that for this specific surface roughness the flow has already entered in the transcritical regime and thus, the boundary layer should

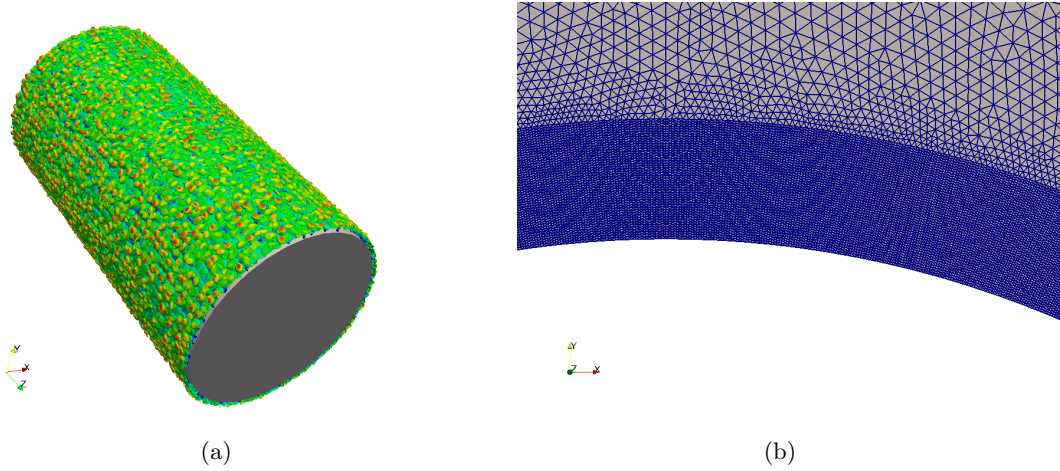


Figure 2. (a) Visualization of the sand-grain surface coloured by k_s/r ; (b) Detail of the mesh in near the wall.

be turbulent before separation [14] in contrast with the smooth cylinder which the flow should correspond with the critical regime [2].

The case is solved in a computational domain of dimensions $x \equiv [-10D : 20D]$; $y \equiv [-10D : 10D]$ in the stream-wise and cross-stream directions and two different span-wise lengths of 0.96 and 1.92, with a circular cylinder of diameter D at $(0,0,0)$. The domain dimensions have been selected based on the experience of the research group with cylinder flows, and is expected to be large enough to contain the largest scales of the flow.

The boundary conditions at the inflow consist of a uniform velocity $(u,v,w)=(1,0,0)$. Constant velocity $(u,v,w)=(1,0,0)$ is also prescribed at the other external boundaries except for the downstream one (outlet) where a pressure-based condition is used. At the cylinder surface, a virtual sandgrain model [27, 20] will be used to impose the roughness. The roughness is modeled by closely spaced, randomly rotated ellipsoids with semi-axes k_s/D , $1.4k_s/D$ and $2k_s/D$. A detail of the resulting sand-grain roughness surface is depicted in figure 2(a). Previous work by [20] has determined the maximum grid spacing required to represent this surface accurately, and the computational mesh will be designed to satisfy these requirements. A prism layer will be constructed around the cylinder surface, extending up to the edge of the roughness sublayer $\sim 3k_s/D$. Beyond that distance from the wall an unstructured grid will be used. Each roughness element will be resolved by $n_\theta \times n_z$ cells (see Table 1) of the superficial mesh with 30 – 50 points below the roughness crest in the radial direction.

The use of an unstructured mesh in the outer region will allow to cluster more control volumes close to the cylinder and in the near wake, whereas away from the region of interest, the mesh requirements can progressively be relaxed (see figure 2(b)). An approximate estimate of the mesh required is given in Table 1. Note that the main constraint is the grid spacing imposed by the roughness element size, rather than by the turbulence structure; thus the grids for cases 1-3 will be nearly the same, whereas a finer grid will be necessary for the two higher Reynolds numbers.

For this particular case, two different grids have been solved; the grid characteristics are given in table 1.

The cases are simulated for a sufficiently long period of time to guarantee converged statistics. An initial transient of roughly 60 times units ($TU = tU_{ref}/D=60$) is *a priori* estimated. After the initial transient, statistics are collected for about $TU = 120$ (about 25 shedding cycles), which are sufficient to ensure converged statistics.

Table 1. Meshes studied. NCV_{total} is the total number of control volumes; NCV_{plane} is the total number of control volumes in the plane; N_{planes} is the total number of planes in the spanwise direction; N_θ , N_z are the total number of sandgrain elements in the radial and spanwise directions; n_θ , n_z are the average mesh resolution for each roughness element; L_z is the spanwise size of the domain; $n_y^{3k_s}$ is the number of grid points in the wall normal direction within a $3k_s/D$ distance.

case	NCV_{total} $\times 10^{-6}$	NCV_{plane}	N_{planes}	$N_\theta \times N_z$	$n_\theta \times n_z$	L_z	$n_y^{3k_s}$
M0	41.77	217594	192	78.5×24	8×8	0.96	30
M1	219.38	285658	768	78.5×48	16×16	1.92	50

Table 2. Flow parameters. Comparison with literature available numerical and experimental results. C_D drag coefficient, $C_{D,rms}$ fluctuating drag, $C_{L,rms}$ fluctuating lift, St non-dimensional vortex shedding frequency. †LES for a smooth cylinder [2, 9], *Experimental results for roughened cylinders with $k_s = 4.5 \times 10^{-3} - 3 \times 10^{-2}$ [13, 14, 7, 29]

Re	C_D	$C_{D,rms}$	$C_{L,rms}$	St
4.2×10^5 (M0)	1.141	0.094	0.523	0.211
4.2×10^5 (M1)	1.122	0.080	0.445	0.204
5.3×10^5 (smooth)†	0.296	0.011	0.071	0.368
(exp)*	0.9-1.3	-	-	0.21-0.24

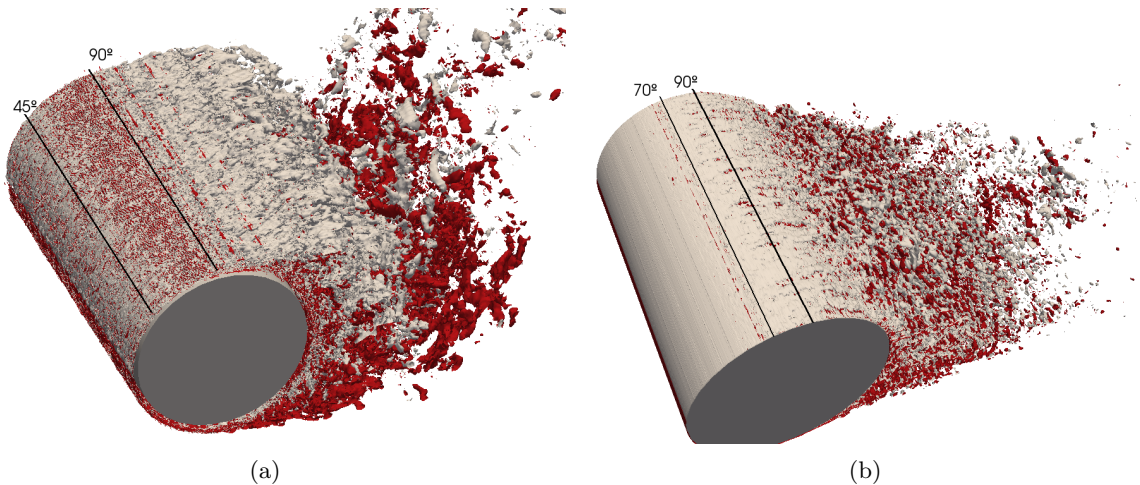


Figure 3. Instantaneous spanwise vortical structures. $\omega_z = \pm 15$. (a) $Re = 4.2 \times 10^5$; (b) $Re = 5.3 \times 10^5$ (smooth cylinder)

4. Results

4.1. Time-average aerodynamic coefficients

4.2. Overview of the instantaneous flow

4.3. Flow parameters and wake topology

A direct comparison of the wake statistics between the rough cylinder and the smooth cylinder is plotted in figures 6 and 7. In the figure, the data of the rough cylinder at $Re = 4.2 \times 10^5$, which is supposed to be in the transcritical regime [14] is compared to those of the smooth cylinder

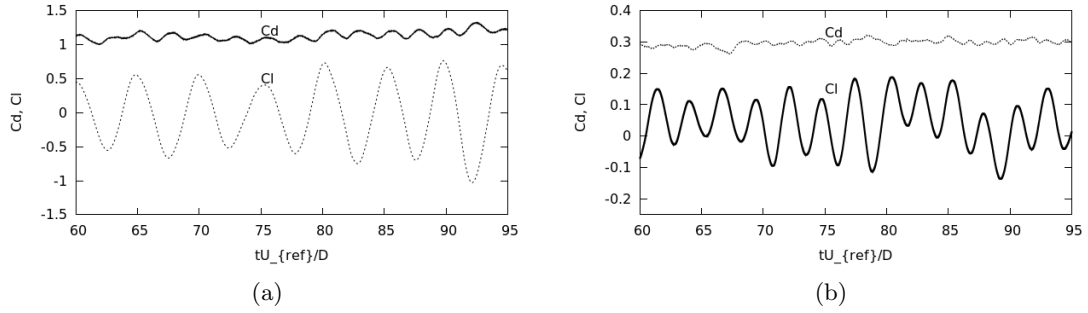


Figure 4. Instantaneous variation of the lift and drag coefficients (a) $Re = 4.2 \times 10^5$; (b) $Re = 5.3 \times 10^5$ (smooth cylinder)

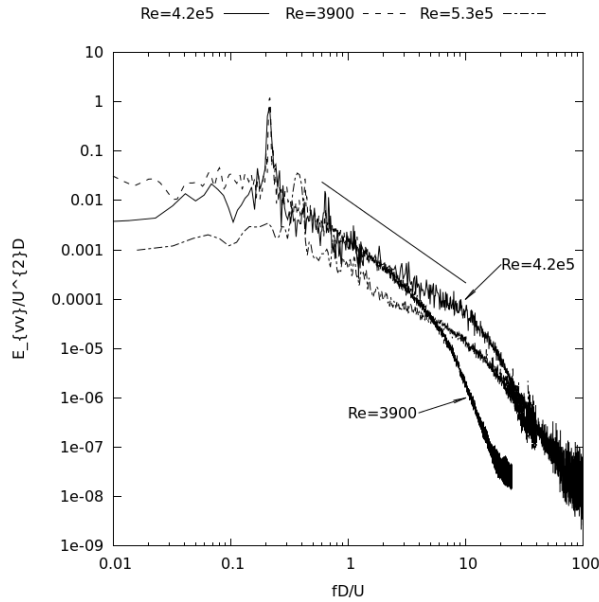


Figure 5. Energy spectrum of the cross-streamwise velocity fluctuations of a numerical probe located in the wake at $x/D = 2$; $y/D = 0.5$

at a comparable Reynolds numbers of $Re = 5.3 \times 10^5$, which is in the critical regime [2] and the smooth cylinder in the subcritical regime at $Re = 3900$ [30]. As depending on the Reynolds numbers, the length of the recirculation region behind the cylinder changes (the distance from the cylinder center to the streamwise location in the wake centreline where the streamwise velocity is zero), to make comparable the flow statistics in the near wake they are plotted at streamwise locations normalized by the length of the recirculation zone. In figures 6 and 7 the statistics are plotted at $x/L_r = 0.5$ and $x/L_r = 1$. The length of the recirculation region is of $L_r/D = 1.395$ at $Re = 4.3 \times 10^5$, $L_r/D = 1.225$ at $Re = 5.3 \times 10^5$ [9] and $L_r/D = 1.86$ at $Re = 3900$ [30].

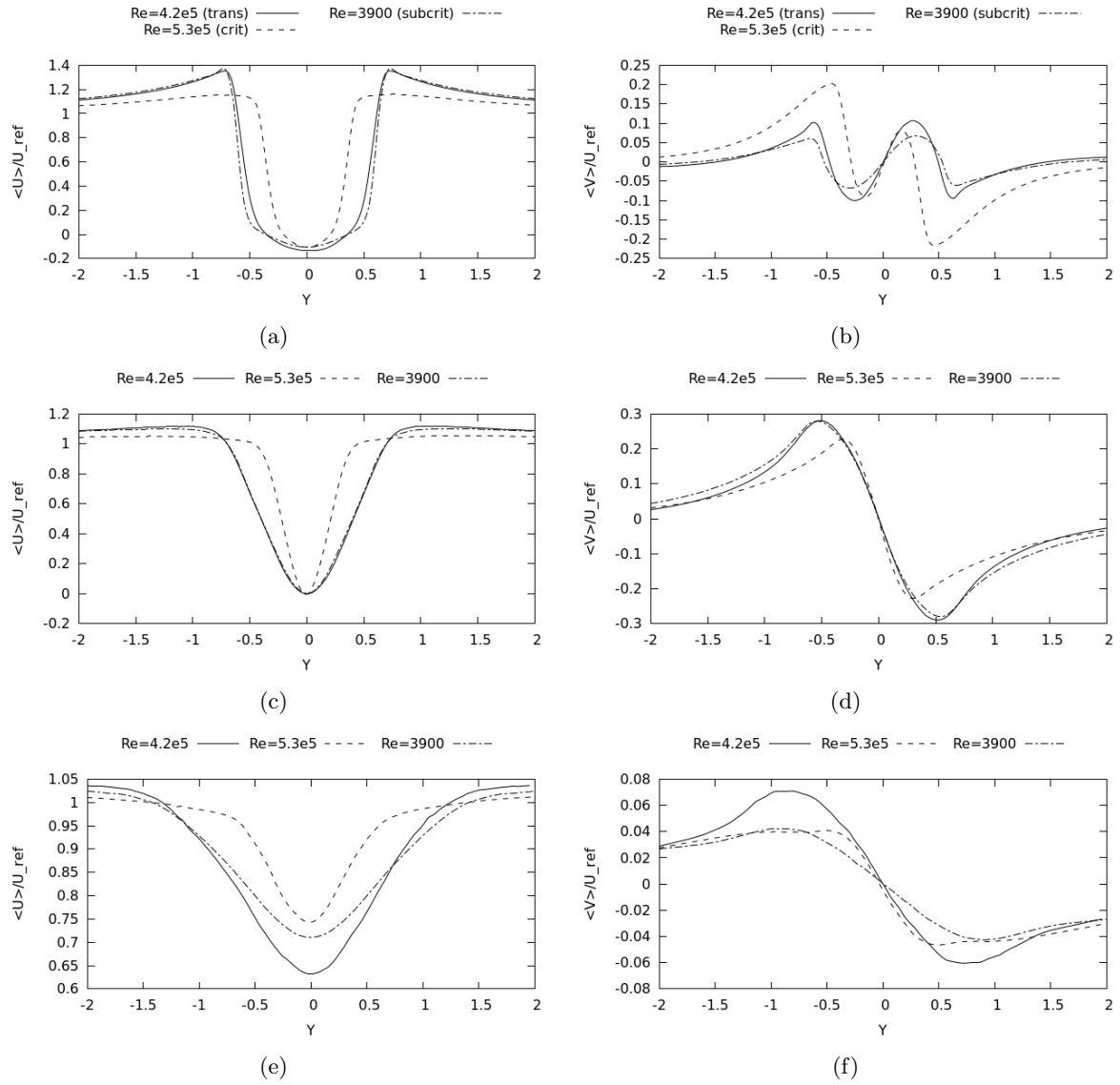


Figure 6. First order statistics in the wake of the cylinder. (a,c,e) Streamwise velocity at $X/L_r = 0.5$, $X/L_r = 1$ and $X/L_r = 2$; (b,d,f) Cross-stream wise velocity at $X/L_r = 0.5$, $X/L_r = 1$ and $X/L_r = 2$

4.4. Concluding remarks

Acknowledgments

This work has been partially financially supported by the Ministerio de Economía y Competitividad, Secretaría de Estado de Investigación, Desarrollo e Innovación, Spain (ref. ENE2014-60577-R) and by the collaboration project between Universitat Politècnica de Catalunya and Termo Fluids S.L. We acknowledge “Red Española de Supercomputación” (RES) for awarding us access to the MareNostrum III machine based in Barcelona, Spain (Ref. FI-2015-2-0026 and FI-2015-3-0011).

References

- [1] C. H. K. Williamson. Vortex dynamics in the cylinder wake. *Annual Review of Fluid Mechanics*, 28(1):477–539, 1996.

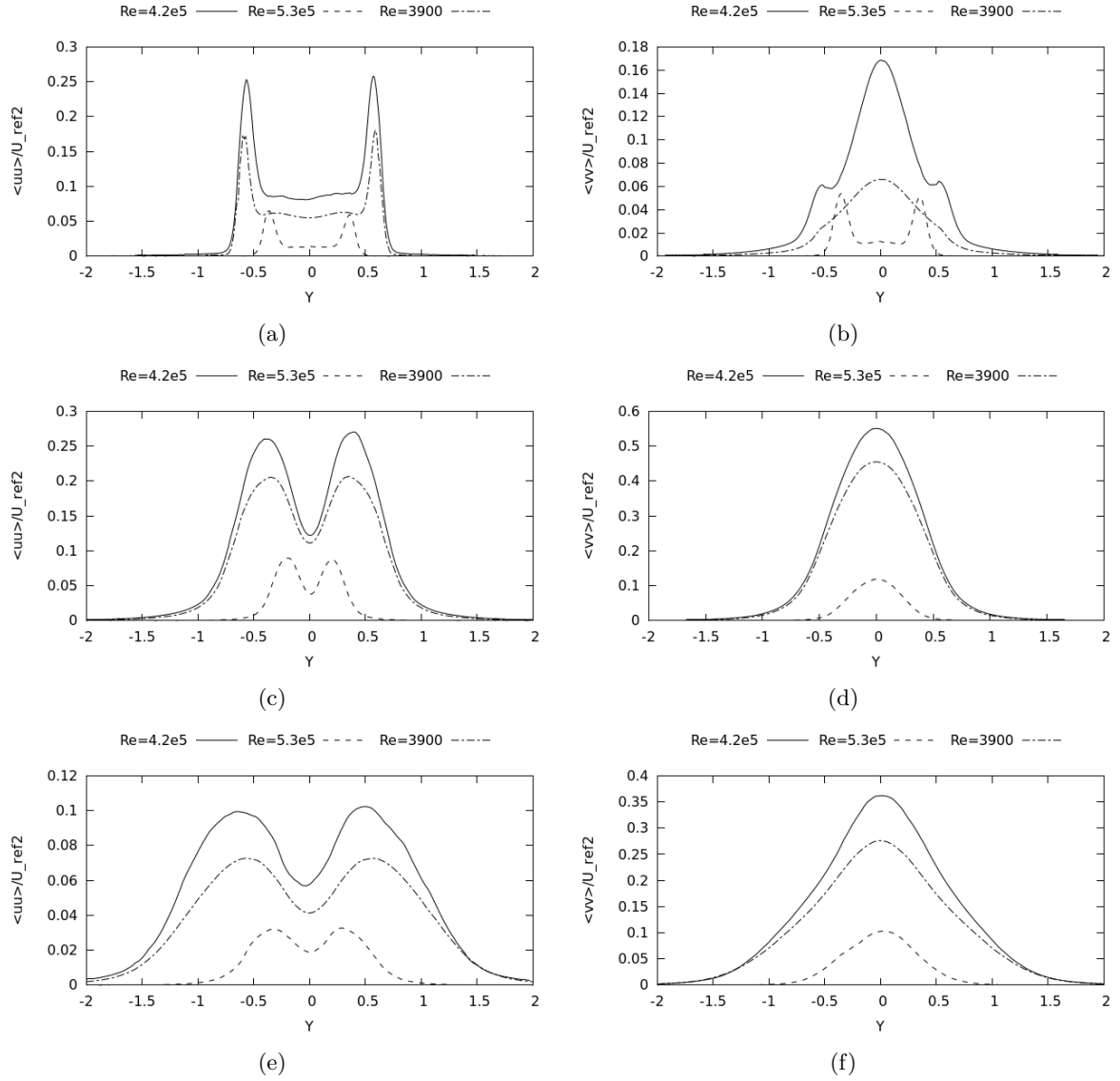


Figure 7. Second order statistics in the wake of the cylinder. (a,c,e) Streamwise velocity fluctuations at $X/L_r = 0.5$, $X/L_r = 1$ and $X/L_r = 2$; (b,d,f) Cross-stream wise velocity fluctuations at $X/L_r = 0.5$, $X/L_r = 1$ and $X/L_r = 2$

- [2] O. Lehmkuhl, I. Rodríguez, R. Borrell, J. Chiva, and A. Oliva. Unsteady forces on a circular cylinder at critical Reynolds numbers. *Physics of Fluids*, 26(12):125110, 2014.
- [3] C Wieselsberger. New data on the laws of fluid resistance. Technical Report TN-84, NACA, 1922.
- [4] A. Fage. Drag of circular cylinders and spheres. Technical Report R&M 1370, Aeronautical Research Council, 1930.
- [5] WJ Bursnall and L.K. Jr Loftin. Experimental investigation of the pressure distribution about a yawed circular cylinder in the critical Reynolds number range. Technical Report NACA TN2463, NACA, 1951.
- [6] NK Delany and NE Sorensen. Low-speed drag of cylinders of various shapes. Technical Report NACA TN3038, NACA, 1953.
- [7] E. Achenbach and E. Heinecke. On vortex shedding from smooth and rough cylinders in the range of Reynolds numbers $6e3$ to $5e6$. *J. Fluid Mech.*, 109:239–251, 1981.
- [8] G Schewe. On the force fluctuations acting on a circular cylinder in crossflow from subcritical up to transcritical Reynolds numbers. *Journal of Fluid Mechanics*, 133:265–285, 1983.

- [9] I. Rodríguez, O. Lehmkuhl, J. Chiva, R. Borrell, and a. Oliva. On the flow past a circular cylinder from critical to super-critical Reynolds numbers: Wake topology and vortex shedding. *International Journal of Heat and Fluid Flow*, 2015.
- [10] M. R. Raupach, R. A. Antonia, and S. Rajagopalan. Rough-wall boundary layers,. *Applied Mechanics Review*, 44:1–25, 1991.
- [11] J. Jimenez. Turbulent Flows Over Rough Walls. *Annual Review of Fluid Mechanics*, 36(1):173–196, 2004.
- [12] Karen A. Flack and Michael P. Schultz. Roughness effects on wall-bounded turbulent flows. *Physics of Fluids*, 26(10):101305, 2014.
- [13] A. Fage and J.H. Warsap. The effects of turbulence and surface roughness on the drag of a circular cylinder. Technical Report R&M 1283, Aeronautical Research Council, 1930.
- [14] E Achenbach. Influence of surface roughness on the cross-flow around a circular cylinder. *Journal Fluid Mechanics*, 46(2):321–335, 1971.
- [15] E. C. Polhamus. A review of some Reynolds number effects related to bodies at high angle of attack. Technical Report NASA Contractor Report 3809, NASA, 1984.
- [16] E Szechenyi. Supercritical Reynolds number simulation for two-dimensional flow over circular cylinders. *Journal of Fluid Mechanics*, 70:529–542, 1975.
- [17] O. Güven, C. Farrell, and V. C. Patel. Surface-roughness effects on the mean flow past circular cylinders. *Journal of Fluid Mechanics*, 98(4):673, 1980.
- [18] W.C.L. Shih, C. Wang, D. Coles, and A. Roshko. Experiments on flow past rough circular cylinders at large Reynolds numbers. *Journal of Wind Engineering and Industrial Aerodynamics*, 49:351–368, 1993.
- [19] A. Leonard. Energy cascade in large-eddy simulations of turbulent fluid flows. *Adv. Geophys.*, 18A:237–248, 1975.
- [20] J. Yuan and U. Piomelli. Numerical simulations of sink-flow boundary layers over rough surfaces. *Physics of Fluids*, 26(1), 2014.
- [21] F. Nicoud and F. Ducros. Subgrid-scale stress modelling based on the square of the velocity gradient tensor. *Flow, Turbulence and Combustion*, 62:183–200, 1999.
- [22] L. Jofre, O. Lehmkuhl, J. Ventosa, F. X. Trias, and A. Oliva. Conservation properties of unstructured finite-volume mesh schemes for the Navier-Stokes equations. *Numerical Heat Transfer, Part B: Fundamentals*, 54(1):53–79, 2014.
- [23] F. X. Trias, O. Lehmkuhl, A. Oliva, C. D. Pérez-Segarra, and R. W. C. P. Verstappen. Symmetry-preserving discretization of Navier-Stokes equations on collocated unstructured grids. *Journal of Computational Physics*, 258:246–267, 2014.
- [24] F. X. Trias and O. Lehmkuhl. A self-adaptive strategy for the time integration of Navier-Stokes equations. *Numerical Heat Transfer. Part B*, 60(2):116–134, 2011.
- [25] I. Rodríguez, R. Borrell, O. Lehmkuhl, C. D. Pérez-Segarra, and A. Oliva. Direct numerical simulation of the flow over a sphere at $Re = 3700$. *Journal of Fluid Mechanics*, 679:263–287, 2011.
- [26] R. Borrell, O. Lehmkuhl, F. X. Trias, and A. Oliva. Parallel direct Poisson solver for discretisations with one Fourier diagonalisable direction. *Computational Physics*, 230(12):4723–4741, 2011.
- [27] A. Scotti. Direc numerical simulation of turbulent channel flows with boundary roughned with virtual sandpaper. *Physics of Fluids*, 18:031701, 2006.
- [28] J. Yuan and U. Piomelli. Estimation and prediction of the roughness function on realistic surfaces. *Journal of Turbulence*, 15(6):350–365, 2014.
- [29] Guido Buresti. the Effect of Surface Roughness on the flow regime around circular cylinders. *Journal of wind engineering and industrial Aerodynamics*, 8:105–114, 1981.
- [30] O. Lehmkuhl, I. Rodríguez, R. Borrell, and A. Oliva. Low-frequency unsteadiness in the vortex formation region of a circular cylinder. *Physics of Fluids*, 25:085109, 2013.